APL Electronic Devices

RESEARCH ARTICLE | FEBRUARY 06 2026

Aerosol jet co-printing for flexible and conductive protein–metal electrodes

Yannan Zhou ; Georgina H. Burgoyne Morris ; Daniel V. Bax ; Sohini Kar-Narayan ; Malavika Nair

APL Electronic Devices 2, 016112 (2026)
https://doi.org/10.1063/5.0300123

APL Electronic Devices ARTICLE pubs.aip.org/aip/aed

Aerosol jet co-printing for flexible and conductive protein–metal electrodes

Cite as: APL Electron. Devices 2, 016112 (2026); doi: 10.1063/5.0300123
Submitted: 31 August 2025 • Accepted: 30 December 2025 •
Published Online: 6 February 2026

Yannan Zhou,[1] Georgina H. Burgoyne Morris,[1] Daniel V. Bax,[1] Sohini Kar-Narayan,[1] and Malavika Nair[1,2,a)]

AFFILIATIONS

[1] Department of Materials Science and Metallurgy, University of Cambridge, Charles Babbage Road, Cambridge CB3 0FS, United Kingdom
[2] Institute of Biomedical Engineering, Department of Engineering Science, University of Oxford, Marcela Botnar Wing, Windmill Road, Oxford OX3 7LD, United Kingdom

[a)] **Author to whom correspondence should be addressed:** malavika.nair@eng.ox.ac.uk

ABSTRACT

We report a rapid, single-step aerosol jet co-printing method for flexible, conductive collagen–silver electrodes. By simultaneously depositing collagen and silver nanoparticle inks, we achieve tunable conductivity and biocompatibility using short (<5 min) low-temperature (150 °C) curing. The resulting composites exhibit resistivity as low as $\approx 10^{-6}$ Ωm, maintain conductivity under mechanical flexure, and preserve partial protein structure for up to 3 weeks in physiological media. Cell culture studies confirm reduced cytotoxicity at high collagen content, defining a processing window that balances electrical and biological performance. These findings demonstrate that aerosol jet printing co-printing offers a scalable and versatile fabrication strategy for next-generation flexible bioelectronic devices, with electrical and biological performance that can be tuned through material composition and processing parameters.

I. INTRODUCTION

Implantable electronic devices play a central role in modern medicine, enabling therapies ranging from cardiac pacing[1] and neural stimulation to prosthetic control and biosensing.[2–5] Such devices rely on electrodes that must simultaneously deliver electrical stimulation to biological tissue, making high electrical conductivity, mechanical flexibility, and biocompatibility critical material requirements.[6–9] Conventional implantable electrodes, such as platinum,[10,11] platinum–iridium alloys,[11] or ceramic coatings[12,13] like titanium nitride[14,15] and iridium oxide,[16,17] offer excellent corrosion resistance and biochemical stability in physiological environments[18–20] but remain mechanically rigid and bioinert. Their stiffness and poor tissue integration often trigger fibrous encapsulation by surrounding tissue, leading to increased stimulation thresholds and reduced device longevity.[6] Silver offers one of the highest electrical conductivities among metals at low processing temperatures, making it attractive for use in flexible bioelectronic fabrication and optimization.[6,21,22] However, the potential cytotoxicity from silver ions limits its use in chronic implants. This makes it a promising candidate for early stage fabrication trials, where the primary focus is on optimizing printing parameters rather than long-term biocompatibility.

While significant progress has been made in improving the performance of implantable electrode materials, less attention has been given to fabrication methods that support rapid prototyping, high-resolution patterning, and integration with flexible substrates. Conventional microfabrication techniques, such as photolithography, vacuum deposition, and electroplating, offer high precision but require multistep, cleanroom-based processing, limiting their adaptability to soft substrates and rapid prototyping. In contrast, printing-based additive manufacturing techniques, such as screen or inkjet printing, provide a low-cost alternative but often compromise on resolution, uniformity, or ink compatibility (supplementary material, Table 1).[22–24] These constraints impede rapid prototyping and compatibility with soft, temperature-sensitive materials

required for bioelectronic interfaces, with limitations further compounded by the demand for mechanical flexibility, biocompatibility, and long-term stability in physiological environments.[25–27]

Aerosol Jet Printing (AJP) has emerged as a powerful direct-write technique capable of depositing a wide range of functional inks with micrometer precision (≈10 μm) and viscosities spanning 1–1000 cP.[28] Unlike pre-mixed approaches, AJP enables *in situ* co-printing of multiple inks from independent atomizers (Fig. 1), allowing materials to be mixed only at the nozzle and minimizing issues such as nanoparticle aggregation or protein denaturation.[29–31] Its compatibility with low-temperature curing allows direct printing onto soft polymeric substrates without significant thermal damage, including proteins such as collagen,[32–34] while its ability to integrate multiple functional materials in a single step streamlines the fabrication process.[30] This unique capability allows direct patterning of metallic nanoparticles and biological materials onto flexible, thermally sensitive substrates. Moreover, its non-contact, maskless operation supports rapid design iteration and scalable fabrication of bioelectronic interfaces.

In this study, AJP is employed in a co-printing configuration with a pneumatic atomizer for silver nanoparticle (AgNP) ink and an ultrasonic atomizer for collagen ink. By co-depositing collagen

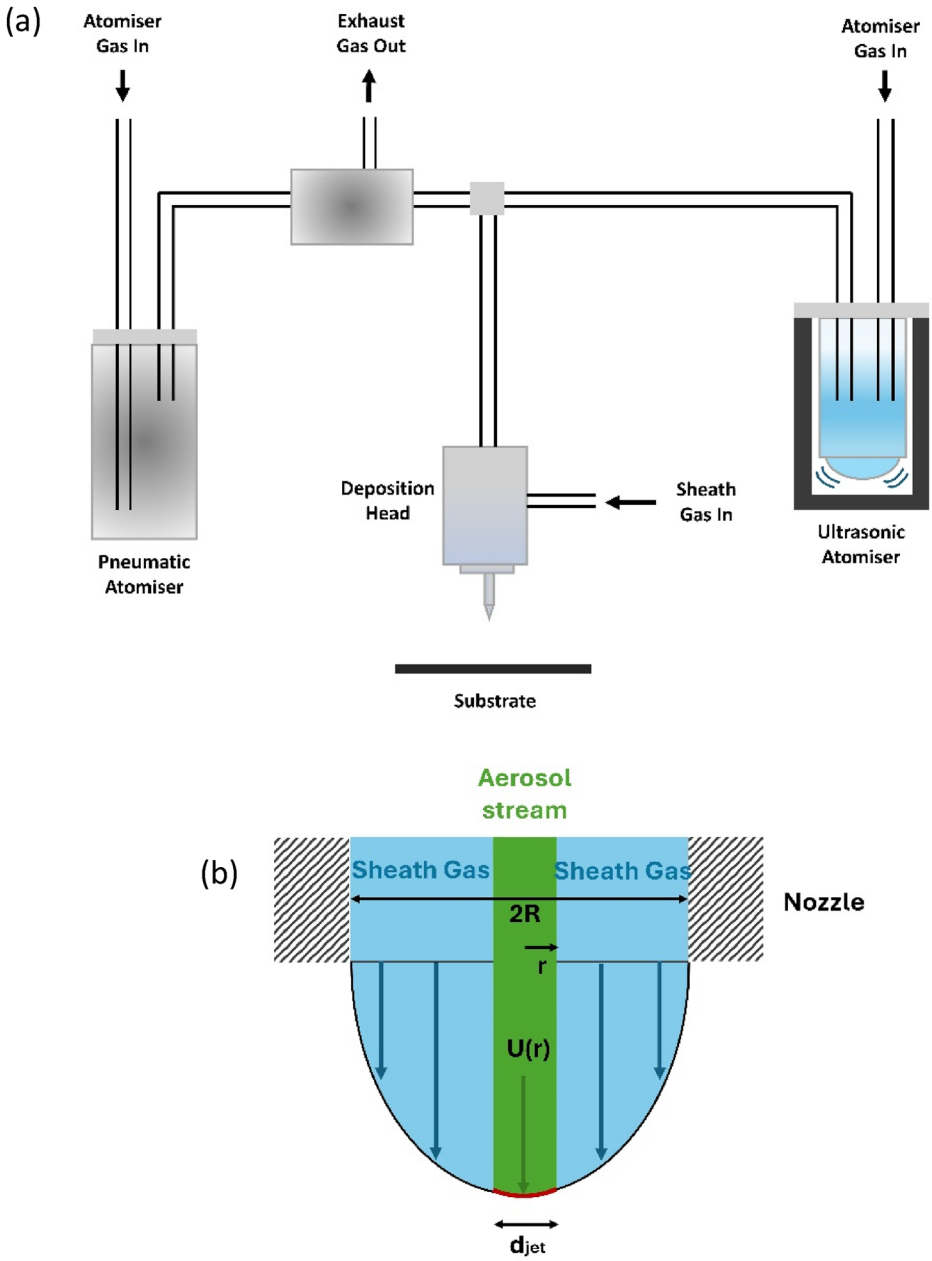

FIG. 1. (a) Schematic of the co-printing process in aerosol jet printing. The AgNP and collagen inks were placed in separate containers and printed out together. A Y-connector was used to mix two gases together toward the deposition head. (b) Schematic of the flow profile at the exit of the print nozzle. The green area displays the aerosol jet stream, and the blue areas display the sheath gas.

and silver nanoparticle (AgNP) inks, we establish how processing parameters, particularly atomizer flow rates and curing conditions, govern print morphology, conductivity, flexibility, and biocompatibility. We identify a short-duration, low-temperature curing regime (150 °C, 2 min) that achieves high conductivity while preserving collagen integrity, and we show that electrode performance can be modulated to balance mechanical compliance and cellular compatibility. The resulting AgNP–collagen composites are finely dispersed during printing, offering tunable conductivity, flexibility, and biological performance without the need for post-processing or complex assembly. In this study, we focus on developing short-term, partially degradable, transient AgNP-collagen composite electrodes, with the aim of enabling temporary biocompatible electrical interfaces.

II. MATERIALS AND METHODS

A. Aerosol jet printing

All samples were co-printed by aerosol jet printing (Optomec) on polyimide substrates (Kapton, 200 μm thickness) with a pneumatic atomizer (PA) for silver nanoparticle (AgNPs) inks (NovaCentrix, diluted 1:2 by volume with deionized water) and an ultrasonic atomizer (UA) for collagen inks, unless stated otherwise. Collagen inks were prepared as a 0.5 wt. % suspension of Type I bovine dermal collagen (Devro Medical) hydrated overnight in 0.05M acetic acid, then blended at 20 000 rpm for 2 min, rested for 1 min, and blended at 22 000 rpm for a further 2 min.

Co-printing was achieved using a Y-connector to merge the PA and UA ink streams, enabling *in situ* mixing of AgNPs and collagen to form a uniform aerosol dispersion. The AJP platen was set at room temperature, and ultrasonic inks were chilled at 20 °C to prevent collagen denaturation. A sheath gas flow of 75 SCCM and a print speed of 1 mm s^{-1} were used with a nozzle of 300 μm diameter to print continuous lines as in Fig. 2(a).

1. Single-layer prints

An initial batch of pure collagen, pure silver, and collagen-silver co-print samples was fabricated for use in general characterization and the degradation study. Oven curing was carried out at 150 °C for 5 h. Further samples consisting of a single-layer co-print were printed with the PA exhaust flow rate reduced to 575 SCCM. Samples were then subjected to one of three oven curing treatments: 70 °C for 24 h, 150 °C for 12 h, or 200 °C for 2 h.

2. Multilayer curing

To further amplify the influence of silver atomization, a multilayer configuration was used, which allows control of Ag aerosol on a consistent collagen-Ag underlayer on the substrates. This design ensures that variations in resistivity arise primarily from the printing itself instead of differences in substrates due to minor differences. Three distinct multilayer electrode designs (Designs A–C) were fabricated, as illustrated in Fig. 2(b). Designs A and B were

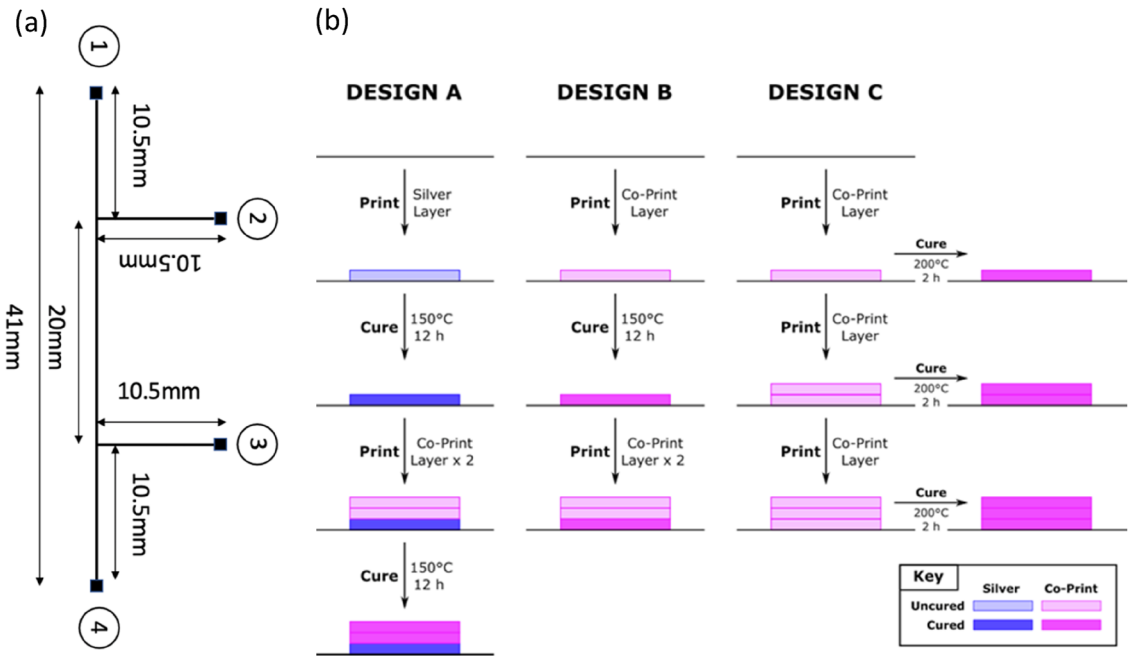

FIG. 2. Schematic illustration of the (a) electrode geometries and (b) three multilayer electrode designs (A–C) fabricated via aerosol jet printing. Designs A and B were printed with the platen temperature set to 70 °C. In Design A, the silver nanoparticle layer was deposited using a UA carrier gas flow rate of 2 SCCM. All co-printed layers in Designs A and B used a UA carrier gas flow rate of 32 SCCM and a PA atomizer and exhaust flow rate of 600 SCCM. For Design C, the PA atomizer flow rate was increased to 700 SCCM across all layers to assess the impact of enhanced atomization on print morphology and electrical performance.

printed with the platen temperature set to 70 °C. For Design A, the silver nanoparticle layer was deposited using a UA carrier gas flow rate of 2 SCCM. All co-printed layers in Designs A and B were printed using a UA carrier gas flow rate of 32 SCCM, with the PA atomizer and exhaust flow rates maintained at 600 SCCM. A multilayer configuration was selected because conductivity in AgNP–collagen composites requires sintering a base silver-rich layer, whereas collagen-containing surface layers must remain uncured to maintain their structural integrity. Single-layer films cannot decouple these requirements, as curing conditions sufficient to sinter AgNPs simultaneously denature collagen. The multilayer architecture, therefore, enables meaningful comparison of nanoparticle percolation while preserving the biointerface. This multilayer strategy was selected because it allows atomization conditions to be varied while maintaining a controlled composite composition across layers, which is not achievable in single-layer films.

Design A was intended to examine the effect of reduced silver atomization (UA 2 SCCM) on film continuity, with a pure Ag layer used intentionally to isolate the effect of severely reduced Ag aerosolization (UA 2 SCCM) on nanoparticle percolation without the additional variable of collagen distribution. Specifically, the pure Ag base layer in Design A ensured that changes in resistivity arose from atomization settings rather than compositional differences. Design B maintained identical parameters to Design A except for the full co-printing of both inks (UA 32 SCCM) to assess interface quality. Design C increased PA flow (700 SCCM) to test whether enhanced aerosolization improves AgNP dispersion and conductivity.

3. Variable collagen/AgNP prints

To investigate the effect of variable collagen/AgNP ratios, electrodes with three layers were printed for each electrode to ensure continuity in the printed lines. Four replicates were printed for each condition, as listed in Table I.

TABLE I. Gas flow pressures used in aerosol jet printing of samples, quoted in square cubic centimeters per minute (SCCM).

	Gas flow rate (SCCM)		
Printing condition	Ultrasonic atomizer (UA)	Pneumatic atomizer (PA)	Pneumatic atomizer (PA) exhaust
UA04	4	700	650
UA08	8	700	650
UA12	12	700	650
UA16	16	700	650
UA20	20	700	650
UA24	24	700	650
UA28	28	700	650
UA32	32	700	650
PA500	32	500	450
PA300	32	300	250
PA100	32	100	50

B. Print morphology and quantitative metrics

1. Scanning electron microscopy

Scanning electron microscopy (SEM) was carried out on single layer prints using a Hitachi TM3030Plus desktop SEM in backscattered electron mode for imaging with an electron acceleration voltage of 5 and 15 kV for optimized co-prints. SEM images were analyzed and processed using ImageJ. A Hitachi TM4000Plus desktop SEM was used for energy dispersive x-ray (EDX) analysis of degradation in single-layer print samples with an electron acceleration voltage of 5 kV.

2. Line width quantification

SEM images (3 random fields per sample, n = 3 prints/condition) were analyzed in ImageJ using threshold-based edge detection. Linewidth was measured randomly along a 400 μm segment.

C. Degradation study

As an analog for physiological conditions, single layer print samples were placed in bijou tubes containing 30 ml phosphate-buffered (PBS) solution (137 mM sodium chloride, 10 mM phosphate buffer, 2.7 mM potassium chloride, Fisher Bioreagents™) within an incubator at 37 °C at 11 time points between 1 h and 12 weeks. Ultraviolet–visible (UV–Vis) spectroscopy was performed on the supernatant using a Perkin Elmer Lambda 25 spectrophotometer, in the range of 190–700 nm at intervals of 1 nm.

D. Electrical measurements

Sample resistances were measured in their as-printed state and under concave and convex curvature using a Sciospec ISX-3 impedance analyzer at 100 kHz in a two-point configuration. Silver conductive paint (Electrolube SCP03B; ~5 Ω per contact) was applied to contact points to facilitate measurement, with contact resistance considered negligible. By default, measurements were taken across contacts 1 and 4 and in addition across contacts 2 and 3 [Fig. 2(a)].

To induce curvature, optimized three-layer co-printed electrodes of varying collagen content were printed on Kapton substrates and mounted onto hollow cylinders with inner diameters ranging from 10 to 30 mm and outer diameters from 10 to 40 mm, enabling both convex and concave configurations.

Cross-sectional areas were measured using profilometry (Dektak, Veeco) using a stylus radius of 12.5 μm, a scan time of 30 s, a scan length of 2000 μm, a stylus force of 5 mg, a measurement range of 65 500 nm, and a resolution of 0.222 μm/sample.

Resistivity was calculated as

$$\rho = R\frac{A}{L}, \tag{1}$$

where ρ is the resistivity, R is the resistance, A is the cross-sectional area, and L is the length of the electrode. Resistivity values are quoted as the mean ± the standard deviation across measured values.

E. Nanoindentation

Mechanical properties were assessed via nanoindentation using an iNano system with a target load of 5 mN and a maximum

indentation depth of 1000 nm. The surface approach distance was set to 2000 nm, with a strain rate of 0.2 s^{-1} and a target dynamic displacement of 2 nm. The data are represented as an average of 20 indentation points per condition, measured in triplicate. Young's modulus was extracted from the unloading stiffness using the Oliver–Pharr model[35]

$$E_r = \frac{S}{2\beta\sqrt{\pi A}}, \tag{2}$$

with $\beta = 1.034$, and area function calibrated on fused silica. The sample modulus was obtained from $\frac{1}{E_r} = \frac{1-\nu_s^2}{E_s} + \frac{1-\nu_i^2}{E_i}$ with $\nu_s = 0.3$. We excluded pop-ins and outliers by median absolute deviation.

F. Cytotoxicity assessment

1. Sample fabrication

Optimized tri-layered co-prints of varying collagen content were printed for cell culture (N = 6) on glass cover slips as detailed previously, in addition to silver-only and collagen-only electrodes as controls.

2. Cell culture and seeding

Human dermal fibroblast cells (Sigma-Aldrich) were cultured in Dulbecco's modified Eagle medium (DMEM, Sigma-Aldrich) supplemented with 10% (v/v) fetal bovine serum (FBS, Sigma-Aldrich) and 1% (v/v) penicillin/streptomycin (Sigma-Aldrich) at 37 °C, 5% CO_2. Samples were placed in a 24-well plate and seeded with 2.64×10^4 cells per well, followed by incubation over a 24-h period for live dead staining and a 5-day period for cell morphology.

3. Live-dead staining

Samples were stained using Calcein AM (live) and propidium iodide (dead) (Thermo Fisher) after 24 h and were diluted in serum-free, phenol-red free DMEM according to the manufacturer's directions. The cell media was removed, and 300 μl of live/dead reagents was added to each well for 30 min at room temperature, under aluminum foil, with gentle rocking. Samples were then imaged on a Zeiss AXIO Observer Z1 fluorescence microscope fitted with an Axiocam 530 camera at ×20 magnification.

4. Cell morphology

On day 5, the cells were fixed with 0.5 ml of 4% (w/w) paraformaldehyde in PBS for 30 min, followed by 3 PBS washes. Samples were stained following a procedure that included the addition of 1 ml of 0.5% (v/v) Triton X-100 in PBS solution for ten minutes followed by a PBS wash. The samples were stained with 0.5 ml of the 1:1000 diluted phalloidin in PBS/0.1% Tween solutions and 0.5 ml of the 1:2000 diluted 4′6-diamidino-2-phenylindole (DAPI) solution to stain the actin cytoskeleton and the nucleus, respectively. The samples were then imaged using a Zeiss AXIO Observer Z1 fluorescence microscope fitted with an Axiocam 530 camera at ×20 magnification.

III. RESULTS AND DISCUSSION

A. Print morphology

Micrographs of the collagen (optical), silver, and co-print (SEM) single-layer samples in Fig. 3(a), and full line widths in the supplementary material, Fig. 2, illustrate that film morphology is highly dependent on ink composition. Pure collagen films, imaged optically due to low electron contrast from their polyimide substrate, exhibited significant variation in line widths, with dendritic regions forming at the center of thicker segments and contact pads. These dendrites were also seen to persist after curing, as seen in the supplementary material, Fig. 1. By contrast, pure silver samples displayed significant cracking and local spallation, which were further aggravated by thermal curing. Co-printed samples showed no such cracking was seen in the co-prints, indicating that collagen incorporation mitigates stress-induced delamination and enhances structural integrity.

SEM micrographs of printed tri-layer electrodes under varying collagen contents [Fig. 3(b)] reveal substantial differences in print quality across and within conditions (supplementary material, Fig. 3). At high collagen concentrations, such as UA32, overspray was common, resulting in line widths nearly twice those of other samples. Quantitative analysis of printed line widths reveals a clear, non-linear dependence [Figs. 3(b) and 3(c)]. As the collagen flow is increased from UA04 to UA28, the average linewidth initially decreases from 420 to 240 μm, indicating improved jet focusing and reduced overspray at moderate collagen content, specifically at UA16-24. Beyond UA28, the linewidth increases sharply to ~780 μm, which is consistent with excessive ink viscosity and spreading during deposition. The narrow linewidth deviation from UA04 to UA24 also suggests enhanced print stability under intermediate collagen loading.

Long-term immersion in phosphate-buffered saline (PBS, 37 °C) revealed distinct degradation behaviors for different sample types [Fig. 4(a)]. Optical microscopy revealed that all three single-layer sample types remained broadly intact after 12 weeks in PBS [Fig. 4(a)] with preferential degradation evident in the dendritic regions corresponding to the thickest areas of the sample. (supplementary material, Fig. 4). At higher magnification, the silver-only samples showed minimal morphological change throughout degradation (supplementary material, Fig. 5), although tarnishing was visible at the electrode surfaces, suggesting a mild surface reaction with the PBS medium.

Elemental EDX maps [Figs. 4(b)–4(d)] demonstrate the distribution of silver, sodium, and chlorine before and after degradation. The negligible chlorine content indicates minimal AgCl formation, with the co-localization of chlorine and sodium signals suggesting the deposition of NaCl crystals rather than the formation of silver salts.

B. Optimizing curing conditions

Curing conditions were optimized to achieve silver nanoparticle sintering while preserving collagen structure. Figure 5(a) shows the resistivity of single-layer co-print samples fabricated at a PA exhaust flow rate of 575 SCCM under different thermal treatments. Samples cured at 70 °C for 24 h remained non-conductive, while those cured at 150 °C (12 h) or 200 °C (2 h) achieved conductivity. For the 150 °C cure, 5 out of 6 samples were conductive across all contact pathways, whereas only 3 out of 6 samples cured at 200 °C exhibited similar behavior. Though the average resistivity was lower for the 200 °C samples, sample embrittlement was noted, suggesting collagen denaturation at this temperature.

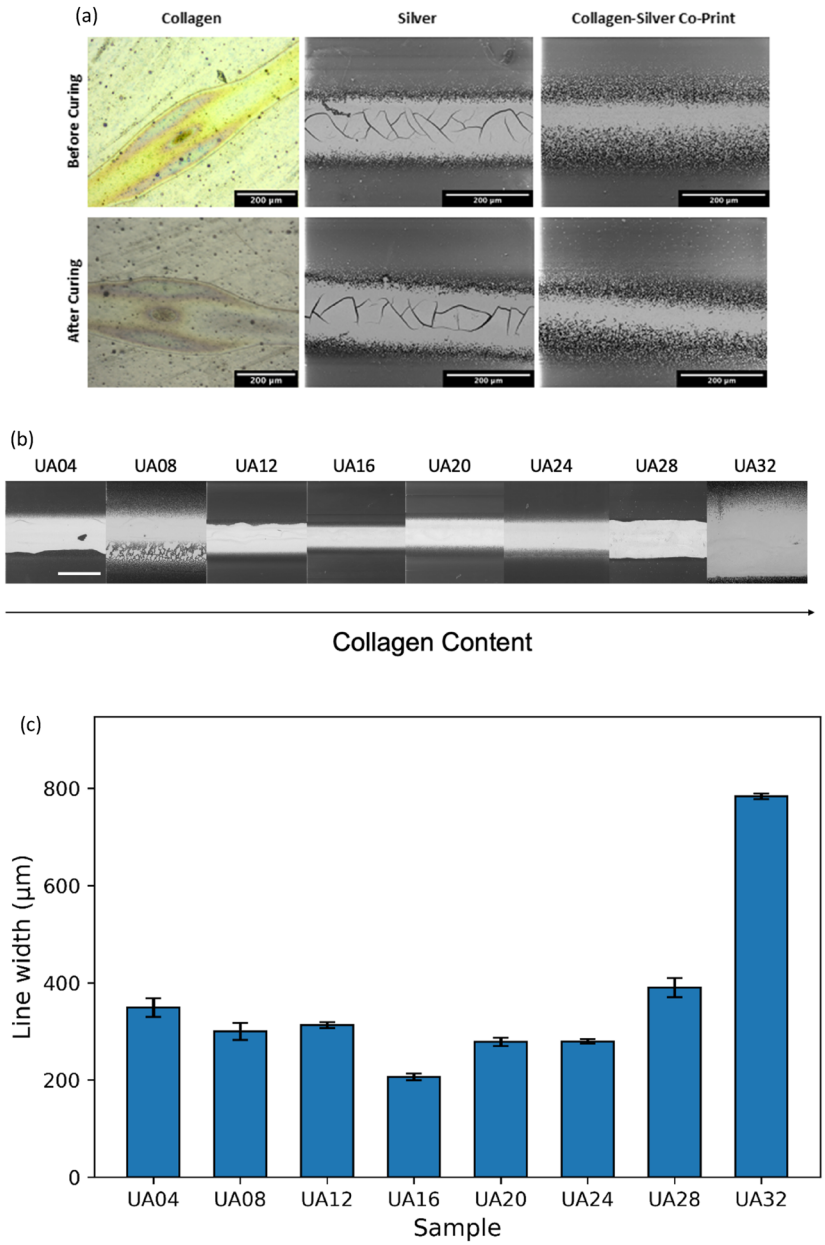

FIG. 3. (a) Optical images of single-layer collagen samples and SEM images of single-layer silver and co-printed samples before and after curing. Pure silver samples displayed significant spallation and cracking, unlike collagen-only or co-printed samples. (b) Tri-layer co-printed electrode lines as a function of increasing collagen flow rates (scale bar: 500 μm). (c) Print linewidth of tri-layer co-printed electrode lines.

Multilayer designs A–C [Fig. 2(b)] exhibited distinct electrical responses. Design A remained non-conductive before and after curing, consistent with its reduced silver aerosolization (UA 2 SCCM), which produced insufficient particle connectivity. Design B, which employed balanced atomization (UA 32 SCCM and PA 600 SCCM), yielded continuous conductive films with a mean resistivity of ± 2 $\mu\Omega$ m. Design C, printed with higher pneumatic atomization (PA 700 SCCM), showed no conductivity prior to curing but achieved conductivity in all two- and three-layer samples after curing, though with higher resistivity and greater variability. Resistivity showed little dependence on layer number, although single-layer samples exhibited larger deviations and outliers [Fig. 5(b)].

Design C samples showed no conductivity prior to curing, but after curing, all two- and three-layer samples were shown to achieve conductivity. Among monolayer samples, four out of six also achieved conductivities upon curing, though two exhibited high resistivity. Resistivity did not vary significantly with the number of layers, but monolayers showed greater variability and outliers [Fig. 5(b)]. This indicates that Design A, printed with minimal Ag aerosolization, produced an insufficiently connected nanoparticle

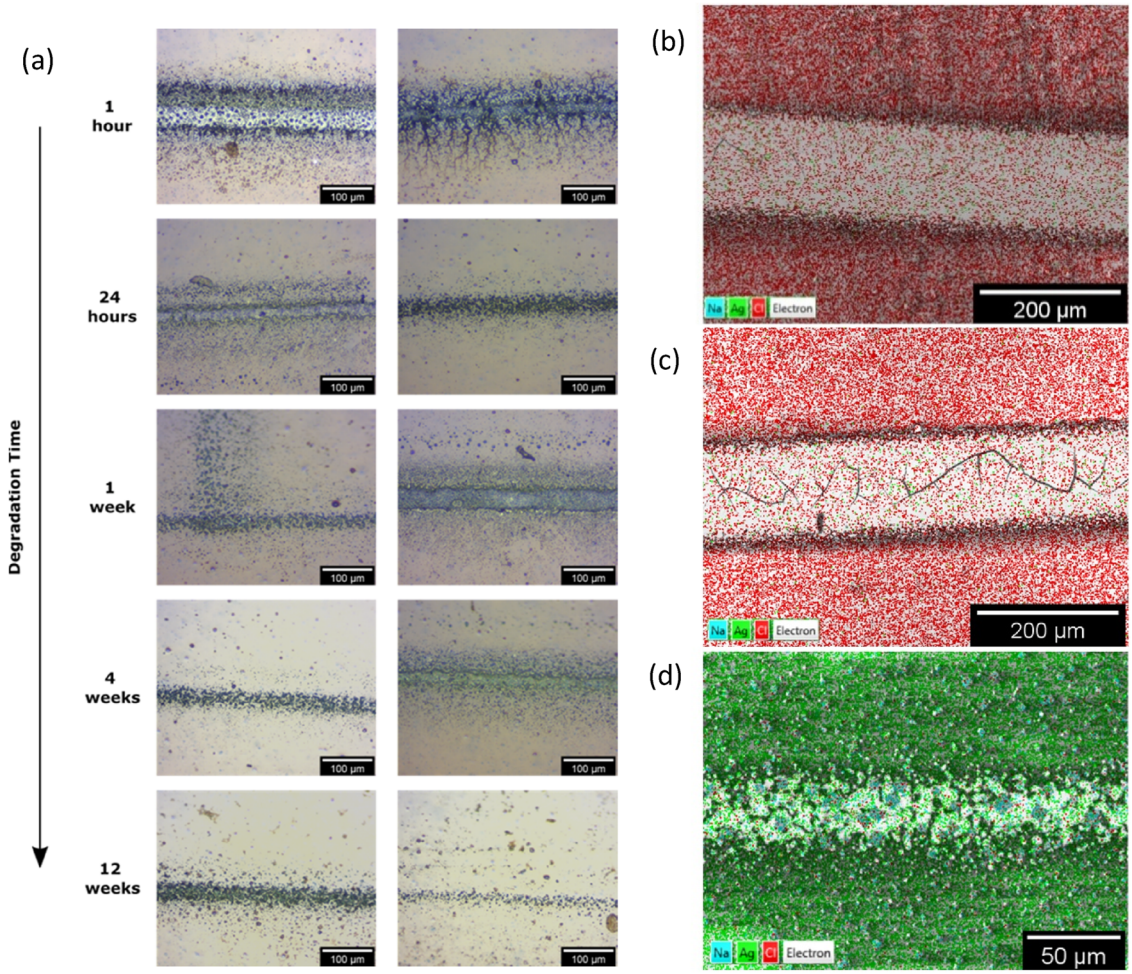

FIG. 4. (a) Optical micrographs of co-print sample degradation over a 12-week period of time in PBS. (b) EDX elemental maps of the distribution of silver and chlorine in silver samples before and (c) after, as well as of silver, sodium, and chlorine in a co-print sample (d) after 12 weeks in PBS solution. Color scheme for EDX maps: (b) and (c) Ag—red, Cl—green, and Na—blue; (d) Ag—green, Na—blue, and Cl—red.

network, while Design C, which used higher pneumatic atomization flow, led to discontinuous percolation. In contrast, Design B yielded continuous and conductive films. This comparison underscores the importance of maintaining ~650 SCCM as the optimal pneumatic atomization pressure for reliable co-printing moving forward.

Tri-layer electrodes printed with UA at 20 SCCM and PA/exhaust at 700/650 SCCM were evaluated for rapid curing under four different thermal conditions. At 150 °C for 5 min, electrodes exhibited low resistance (4.0 ± 0.2 Ω), while a shorter curing time of 2 min at the same temperature resulted in higher resistance (90 ± 5 Ω). Lower temperatures (100–120 °C), even with extended times, failed to produce conductivity. Although prior studies, such as those by Mo *et al.*, have reported that AgNP-based electronics could be rendered conductive at significantly lower sintering temperatures, including 60 °C for 10 min (13.10 $\mu\Omega$ cm) and 100 °C for 10 min (7.40 $\mu\Omega$ cm),[36] lower temperatures of 120 and 100 °C, even with extended curing times, failed to produce conductive samples in this study. The discrepancy in conductivity across the two studies is likely attributed to the presence of collagen in the co-printed samples, which is inherently less conductive than pure AgNP ink.

Although longer exposure (150 °C/5 min) produced marginally lower resistivity, it also caused visible discoloration and embrittlement, consistent with partial collagen denaturation, reducing flexibility and adhesion. Therefore, 150 °C for 2 min was selected as the optimal compromise for subsequent experiments. This curing time is notably shorter than curing protocols reported in previous literature, which typically involve temperatures above 200 °C for durations exceeding 30 min; as a result, efforts have been devoted to seeking alternative sintering strategies.[37] In a prior study by Efimov *et al.*, the authors reported a significant increase in resistivity of aerosol jet printed (AJP) silver layers between 300 and 500 °C, identifying this range as the onset of high conductivity.[38] At lower temperatures (<150 °C), solvent and surfactant removal from the nanoparticle substrate predominates.[38]

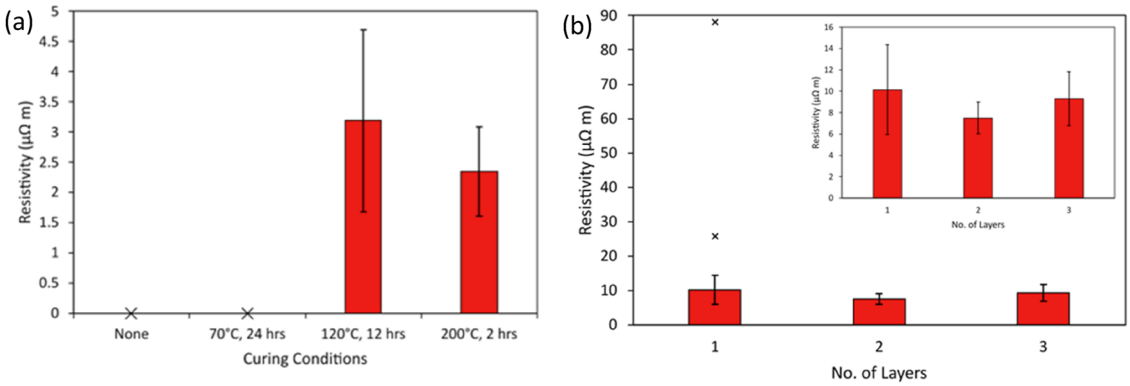

FIG. 5. (a) Resistivity of co-print samples after different heat treatments. Crosses represent non-conductive samples. (b) Resistivity for different numbers of layers in design C multilayer samples. Crosses indicate outlying values. The inset shows the same data on a smaller scale, with outliers excluded.

Although single-layer resistivity measurements are conceptually simpler, they were not used here as reliable comparisons since single-layer co-prints only become conductive at curing temperatures that begin to denature collagen. Multilayer designs were therefore necessary to evaluate atomization behavior while retaining an intact collagen-rich surface.

C. Resistivity of co-prints

To explore the effect of collagen-to-silver ratios, electrodes were fabricated by varying the UA gas flow rate from 4 to 32 SCCM while maintaining a constant PA flow of 700/650 SCCM. Resistance measurements [Fig. 6(a)] were normalized to account for sample geometry, yielding intrinsic resistivity values [Fig. 6(b)] with the measured cross-sectional areas and profiles provided in the supplementary material, Table 1 and Fig. 6.

Although resistivity generally increased with collagen content, the trend was not strictly linear. High conductivity was achieved in electrodes printed with high silver content, corresponding to lower ultrasonic atomizer gas flow rates. Among these, UA04 electrodes exhibited the lowest resistivity of $0.3 \pm 0.1\ \mu\Omega$ m, and PA500 samples (electrodes with higher collagen content) showed the highest resistivity ($378 \pm 103\ \mu\Omega$ m). Although the literature values of bulk silver resistivity at room temperature ($1.59 \times 10^{-2}\ \mu\Omega$ m) or optimized AJP prints of pure silver at ($3.75 \times 10^{-2}\ \mu\Omega$ m) are two orders of magnitude lower than the best values achieved here, the co-prints compare favorably with previous studies, such as the atomic layer deposition of platinum on collagen substrates, which yielded a resistivity of ~2.95 $\mu\Omega$ m.[39] The enhanced conductivity in this study is attributed to the increased incorporation of AgNPs during the printing process.

The stability of these resistances for the single layer prints is further demonstrated in the supplementary material, Fig. 7, which shows the change in resistance per unit length for pure silver and co-printed AgNP–collagen electrodes during immersion in PBS at 37 °C for up to 12 weeks. Silver electrodes maintained their resistance within inter-sample variation, with no statistically significant drift over 1000 h, confirming long-term electrical stability in

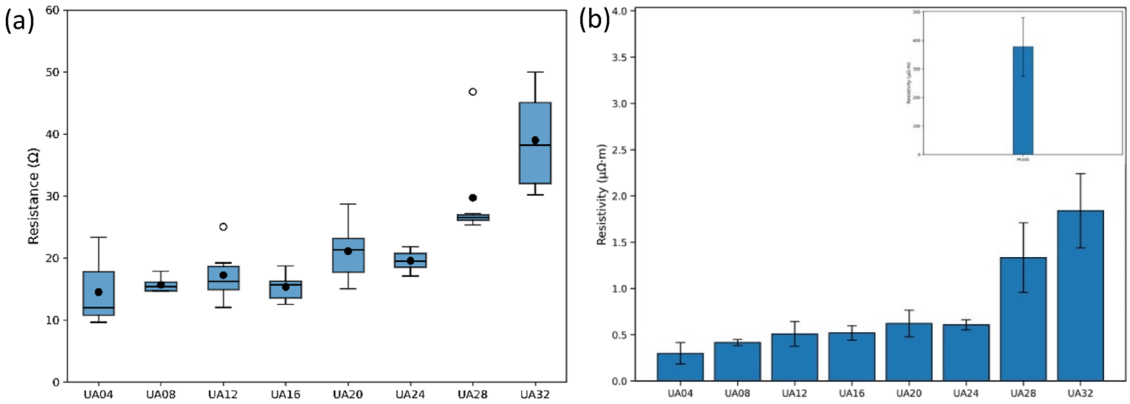

FIG. 6. (a) The resistance of samples printed as a function of increasing collagen content. (b) The dimension-normalized resistivity of electrodes with different printing parameters. The inner box presents the resistivity of PA500, plotted on a separate set of scales for clarity. The error bars represent the standard deviation of each measurement.

physiological media. In contrast, the co-printed electrodes displayed marked temporal variation: resistance increased more than threefold within the first 10 h, then transiently decreased by ~70% over the next 100 h before rising again and eventually becoming nonconductive after ~3 weeks, which indicates partial degradation of the protein matrix and progressive disruption of percolated AgNP pathways. These behaviors are consistent with the transient design intent of composite electrodes, whereas the AgNP only controls remained conductive throughout the 12-week test period. The observed short-term resistivity fluctuations in co-printed composites arise from hydration-driven swelling and partial rearrangement of the collagen matrix, which temporarily alters percolation pathways.

The degradation behavior reported here was obtained from single-layer specimens. Multilayer structures may exhibit different degradation dynamics due to different thickness and composition distribution, and systematic multilayer assessment will be carried out in the future study. In addition, a broader optimization of atomization settings (UA04–UA32 and PA100–PA500) has already been performed, with intermediate collagen content generally showing the most stable resistivity behavior in Fig. 6.

D. Resistivity under flexed loading

To evaluate the mechanical resilience of the co-printed electrodes, samples were mounted onto cylindrical supports of different radii (10–40 mm) to generate controlled concave and convex deformation as shown in the supplementary material, Fig. 8. The resistivity was measured along two orthogonal directions, as illustrated in Fig. 7. The horizontal configuration [Fig. 7(a)] corresponds to the current path parallel to the printed track (contacts 1–4), while the vertical configuration [Fig. 7(b)] corresponds to the perpendicular direction across adjacent printed lines (contacts 2–3).

The results for the UA-series (UA04–UA32) and PA500 samples (Fig. 8) show that resistivity increased moderately with curvature in both orientations. Broken-axis plots were used to accommodate the large difference between PA500 and the UA-series samples.

The PA500 sample, with the highest collagen content, exhibited a markedly higher resistivity compared to the UA-series samples. The complete data of the changes in resistivity with change in curvature is illustrated in the supplementary material, Figs. 9(a)–9(r).

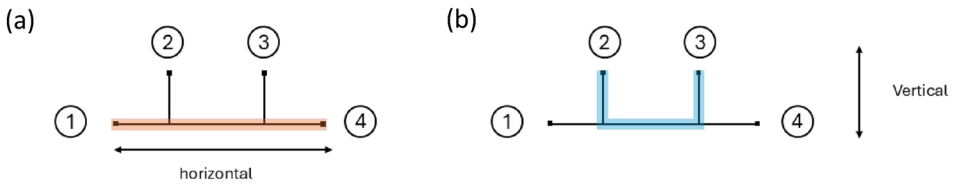

FIG. 7. Direction of electrode flexion test. (a) Measurement along the horizontal direction where current flows along the printed track between contacts 1 and 4. (b) Measurement along the vertical direction, where current flows along the printed track between contacts 2 and 3.

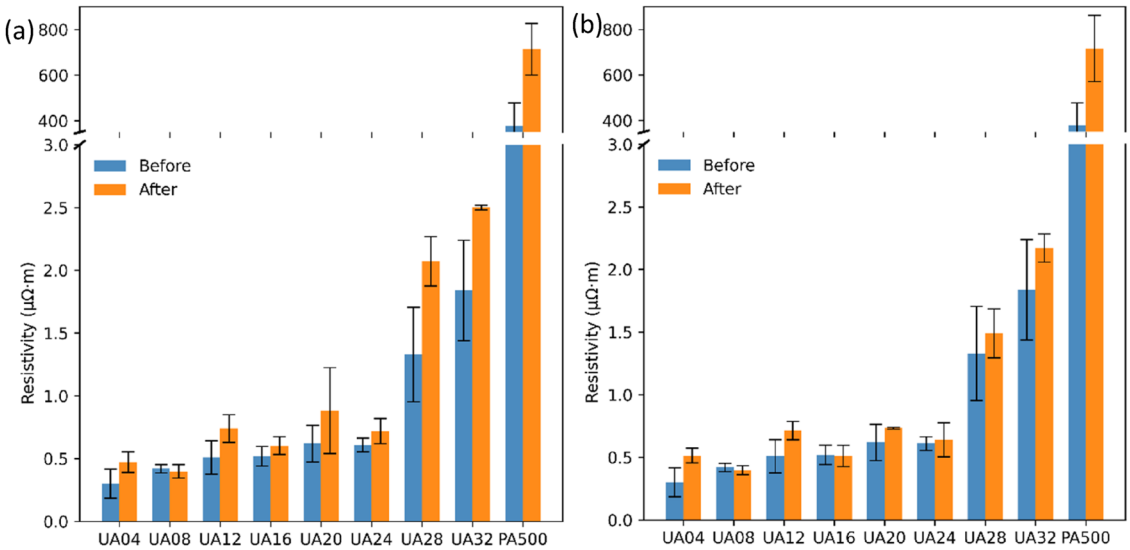

FIG. 8. Broken-axis plots of resistivity ($\mu\Omega$ m) of the samples UA04–UA32 and PA500 before and after treatment in (a) horizontal and (b) vertical directions. The y-axis break was introduced to improve the visualization of the UA-series samples while including PA500 for comparison.

Resistivity in the horizontal direction was consistently 10%–20% higher than in the vertical direction, attributable to greater strain along the current path. SEM images taken before and after bending revealed no new cracks or delamination, confirming structural integrity (supplementary material, Fig. 10). This may be attributed to the mechanical constraint provided by the collagen matrix surrounding the printed AgNPs, stabilizing the printed line. An additional contributing factor might be the short curing duration, which limits the influence of capillary pressure during solvent evaporation and, therefore, the likelihood of crack formation.

E. Nanoindentation

Nanoindentation with the Oliver–Pharr model was carried out to obtain Young's modulus of the co-printed electrodes [Fig. 9(a)]. With increasing collagen content, the modulus decreases from 1.70 GPa (UA04) to 0.39 GPa (UA16), aligning with the mechanical properties of connective tissues such as human tendons (1.0–1.5 GPa) and knee ligaments (3.75–4.3 GPa),[40] or cardiac implants (50–100 kPa). The lowest measured modulus (0.39 GPa) remains significantly higher than the ideal range for neural implants (10^2–10^5 Pa),[41] indicating limited compatibility with soft neural tissues. Beyond UA20, measured modulus values rose again and exhibited higher scatter, likely reflecting inhomogeneous phase separation and localized measurement variability rather than true stiffening. Profilometry (supplementary material, Fig. 6) confirmed Gaussian cross-sectional profiles for the first four conditions, with greater separation and misalignment at higher collagen flows, consistent with decreased uniformity. Despite this variability, all co-printed electrodes were substantially softer than pure AgNP films cured at 150 °C for 30 min (~8.25 GPa)[42] and comparable in stiffness to polymeric encapsulants such as polyimide, parylene C, and PLLA [Fig. 9(b)]. This reduction in modulus enhances mechanical compatibility with soft tissue, an essential factor for flexible or implantable bioelectronics.

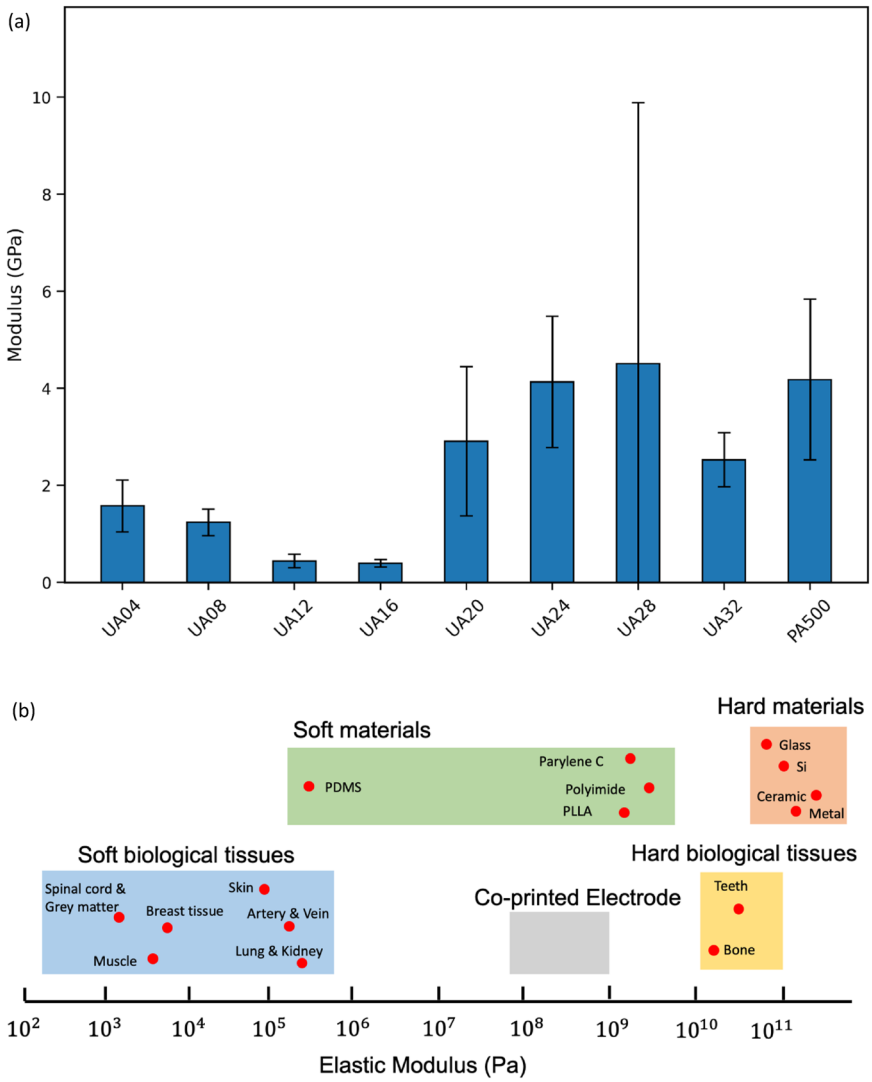

FIG. 9. (a) Elastic modulus of all electrodes. The Young's modulus gradually decreased with increasing collagen content in UA04, UA08, UA12, and UA16, while UA20, UA24, UA28, and UA32 did not show the expected results due to phase separation and localized measurements. (b) Strength ranges of different materials and human tissues.

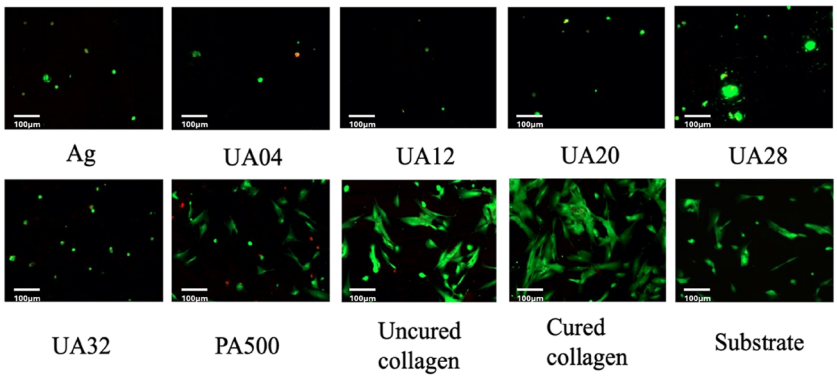

FIG. 10. Live/dead fluorescence images for samples with different silver content after 24 h. Calcein AM (green) represents live cells, and propidium iodide (red) indicates dead cells. Scale bar: 100 μm.

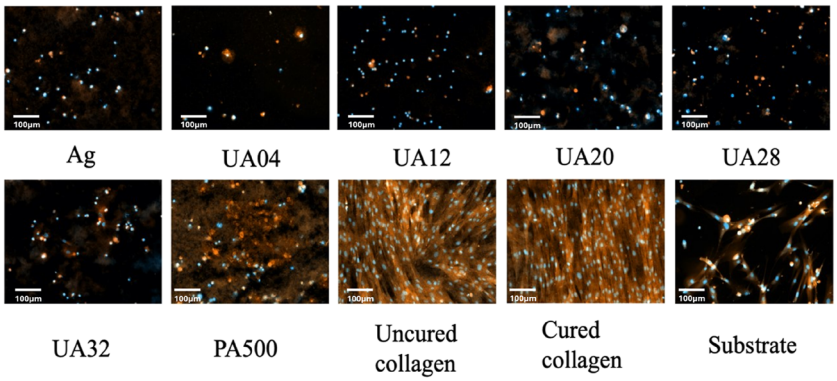

FIG. 11. Fluorescence microscopy images of DAPI/phalloidin staining at day 5 of culture. Phalloidin stained F-actin (orange) and DAPI stained nuclei of a fibroblast (blue). The orange background in PA 500 and UA32 is attributed to collagen autofluorescence. Scale bar: 100 μm.

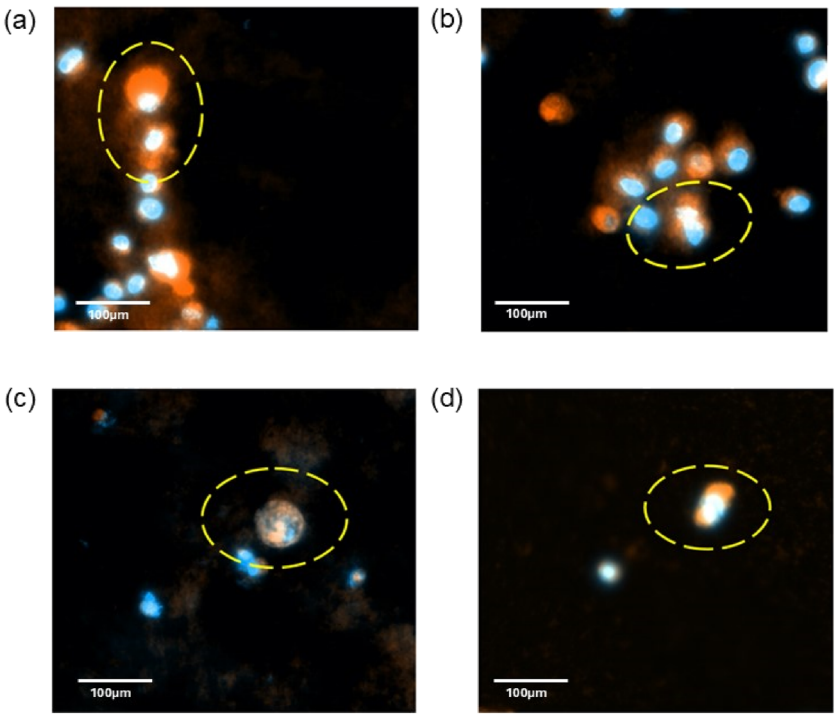

FIG. 12. Magnified view of cells dividing in different samples on day 5. (a) A new nucleus generated in the UA 20 sample, (b) a cell dividing in the UA 12 sample, (c) a pair of nuclei generated in the UA 28 sample, and (d) a cell dividing in the UA 04 sample. Scale bar: 100 μm.

Taken together, these results indicate that intermediate collagen flow rates (UA08-UA16) provide the most favorable balance between modulus and maintained conductivity under our tested conditions.

F. Biocompatibility of co-prints

Live/dead fluorescence assays (Fig. 10) revealed that cell viability was highly dependent on silver concentration. Fibroblasts cultured on collagen-only samples exhibited dense networks of cells with a plump and spindle-shaped morphology indicative of strong adhesion, while silver-rich co-prints supported fewer, rounded cells. No significant cell death occurred within 24 h, but cell density decreased with increasing silver content. Samples with higher collagen fractions (e.g., PA500) showed partial recovery of elongated morphology, suggesting reduced cytotoxicity at lower AgNP loadings.

DAPI/phalloidin staining after 5 days (Fig. 11) confirmed robust attachment and alignment on collagen-only films, while co-printed samples exhibited sparse coverage. On both uncured and cured collagen samples, fibroblast cells exhibited strong attachment, forming a compact monolayer with noticeable alignment along the printed lines. The cytotoxicity in silver containing samples, including cells adhering to glass substrates adjacent to the collagen-silver co-prints, was noted to be affected by the cytotoxicity in the solution environment. This may result from the silver ions released in aerobic environments due to AgNPs oxidation. Analysis of the supernatant using UV–Vis (supplementary material, Fig. 11) for measurable release of AgNPs in the region of 400 nm that is typically observed in the literature[43,44] was not observed for any of the samples in this study. However, the peak at ~230 nm seen for silver samples may be indicative of Ag^+ ions.[45,46] This is consistent with prior experiments by Xu *et al.*, who demonstrated that the oxidative dissolution of silver ions from AgNPs in aerobic environments compared to anaerobic environments may lead to the antibacterial effect of AgNPs, which in this study manifests as potential cytotoxicity in mammalian cells.[47]

Although incremental increases in collagen content from UA04 to UA32 were insufficient to fully restore viability, PA500 samples supported moderate cell proliferation, as evidenced by dividing nuclei (Fig. 12). This suggests that a subset of cells remained metabolically active and proliferative even on day 5 of culture in the high collagen conditions. Yellow-marked regions in Figs. 12(a)–12(d) indicate active mitosis across multiple samples (UA04, UA12, UA20, and UA28). These findings suggest that while AgNP content remains a dominant cytotoxic factor, co-printing at higher collagen ratios can mitigate its effects, providing a tunable balance between conductivity and biocompatibility. PA500, in particular, highlights a processing window where moderate cell viability can be complemented alongside moderate conductivity.

IV. CONCLUSIONS

This study demonstrates the feasibility of fabricating electrically conductive collagen–silver composite electrodes via co-mixed aerosol jet printing. High conductivity was achieved with minimal curing, enabling multilayer designs where only the base layer is cured, preserving collagen integrity at tissue-contacting surfaces. Optimized printing and curing conditions yielded resistivity values as low as $0.3 \pm 0.1\ \mu\Omega$ m, with electrodes maintaining conductivity and flexibility under mechanical deformation. However, biocompatibility remains a challenge, as silver-containing samples showed poor cell adhesion and viability, which was minimized at a specific processing window (PA500) to provide moderate electrical conductivity ($350\ \mu\Omega$ m) alongside viability. Based on nanoindentation results, electrodes printed with intermediate collagen content (UA08–UA16) exhibit reduced modulus values (0.4–1.7 GPa) while maintaining low resistivity, defining a practical processing window for more favorable mechanical behavior as flexible bioelectronic interfaces. Further optimizations of atomization rate and Ag/collagen loading are required to minimize resistivity drift and ensure reliable performance for implantable transient applications. In short, aerosol jet printing has been shown to be a useful technique in rapidly varying material composition and improving nanoparticle distribution, with future avenues exploring alternative conductive materials such as gold or platinum to enhance biological compatibility for the assessment of electrically and biologically compatible electrodes while maintaining flexible electrodes for biological applications.

SUPPLEMENTARY MATERIAL

The supplementary material contains a comparison of techniques for electrode fabrication (Table 1), optical (Fig. 1) and scanning electron micrographs (Fig. 2) of printed single layers, line widths of single prints (Fig. 3), optical micrographs of degrading samples (Figs. 4 and 5), cross-sectional areas and profiles of electrodes with variable collagen concentration (Fig. 6 and Table 2), resistance of silver and co-print samples with degradation (Fig. 7), a schematic of curvature resistance tests (Fig. 8), full figures of resistivity variations with flexion (Fig. 9), SEM images after flexion tests (Fig. 10), and UV–Vis data before and after degradation (Fig. 11).

ACKNOWLEDGMENTS

This study was supported by the Royal Society of Chemistry Research Enablement Grant No. E20-8065. M.N. also acknowledges funding from Emmanuel College and EPSRC New Investigator (Grant No. EP/Y004434/1). D.V.B. would like to acknowledge support from the Cambridge Royce facilities, Grant No. EP/P024947/1, and Sir Henry Royce Institute—recurrent Grant No. EP/R00661X/1. S.K.N. acknowledges funding from UK Research and Innovation (UKRI) under the UK government's Horizon Europe funding guarantee (Grant No. EP/Y032535/1).

AUTHOR DECLARATIONS

Conflict of Interest

The authors have no conflicts to disclose.

Author Contributions

Yannan Zhou: Formal analysis (equal); Investigation (equal); Methodology (equal); Visualization (equal); Writing – original draft

(equal). **Georgina H. Burgoyne Morris**: Formal analysis (equal); Investigation (equal); Methodology (equal); Visualization (equal); Writing – original draft (equal). **Daniel V. Bax**: Methodology (supporting); Resources (equal); Writing – review & editing (equal). **Sohini Kar-Narayan**: Methodology (supporting); Resources (equal); Writing – review & editing (equal). **Malavika Nair**: Conceptualization (lead); Funding acquisition (lead); Supervision (lead); Writing – original draft (supporting); Writing – review & editing (lead).

DATA AVAILABILITY

 The raw data are available on the Oxford University Research Archive (ORA) Data Repository at https://doi.org/10.5287/ora-14x9dqqzp, Ref. 48.

REFERENCES

[1]National Institute for Cardiovascular Outcomes Research, National Cardiac Audit Programme (NCAP) | 2025 Report (2023/24 and 2021/24 Data), 2025, https://www.nicor.org.uk/~documents/route%3A/download/3656.

[2]T. J. Foutz and M. Wong, "Brain stimulation treatments in epilepsy: Basic mechanisms and clinical advances," Biomed. J. **45**(1), 27–37 (2022).

[3]J. Lee, S. Y. Han, and Y. W. Kwon, "Technological advances and medical applications of implantable electronic devices: From the heart, brain, and skin to gastrointestinal organs," Biosensors **15**(8), 543 (2025).

[4]J. Kim, J. Hong, K. Park, S. Lee, A. T. Hoang, S. Pak, H. Zhao, S. Ji, S. Yang, C. K. Chung, S. Yang, and J. Ahn, "Injectable 2D material-based sensor array for minimally invasive neural implants," Adv. Mater. **36**(32), 2400261 (2024).

[5]P. Oldroyd, S. Velasco-Bosom, S. L. Bidinger, T. Hasan, A. J. Boys, and G. G. Malliaras, "Fabrication of thin-film electrodes and organic electrochemical transistors for neural implants," Nat. Protoc. **20**(8), 2100–2124 (2025).

[6]Y. Zhou, G. H. Burgoyne Morris, and M. Nair, "Current and emerging strategies for biocompatible materials for implantable electronics," Cell Rep. Phys. Sci. **5**(8), 101852 (2024).

[7]M. A. Huynh, C.-M. Nguyen, S. Yadav, T. T. H. Nguyen, S. S. Jamali, P. Tanner, T.-K. Nguyen, and N.-T. Nguyen, "Wafer-level fabrication of flexible silicon carbide bioelectronics for electrical stimulations," ACS Appl. Electron. Mater. **7**(18), 8364–8376 (2025).

[8]J. Li, D. Mo, J. Hu, S. Wang, J. Gong, Y. Huang, Z. Li, Z. Yuan, and M. Xu, "PEDOT:PSS-based bioelectronics for brain monitoring and modulation," Microsyst. Nanoeng. **11**(1), 87 (2025).

[9]X. Qian and C. Liao, "Engineering liquid metal-based implantable electrodes toward brain-machine interfaces," Health Sci. Rev. **9**, 100118 (2023).

[10]L.-W. Jang, J.-h. Kim, W. Lee, J.-H. Lee, G.-G. Oh, H. Jung, S.-W. Kim, D.-W. Jeon, T.-Y. Ha, K.-A. Chang, and J. Kim, "Investigation of structural, optical, electrical, and biological properties of a porous platinum electrode for neurostimulation devices," ACS Appl. Bio Mater. **8**(4), 3111–3118 (2025).

[11]A. Petrossians, J. J. Whalen, J. D. Weiland, and F. Mansfeld, "Surface modification of neural stimulating/recording electrodes with high surface area platinum-iridium alloy coatings," in *2011 Annual International Conference of the IEEE Engineering in Medicine and Biology Society* (IEEE, Boston, MA, 2011), pp. 3001–3004.

[12]V. Karamzadeh, H. Yazdani Sarvestani, A. Sohrabi-Kashani, A. Kulkarni, A. Jafari, T. Lacelle, H. Savoji, M. B. Jakubinek, and B. Ashrafi, "Engineering ceramics for biomedical applications through nanofiller integration and 3D printing," Adv. Compos. Hybrid Mater. **8**(2), 223 (2025).

[13]A. Upadhyay, L. Pradhan, D. Yenurkar, K. Kumar, and S. Mukherjee, "Advancement in ceramic biomaterials for dental implants," Int. J. Appl. Ceram. Technol. **21**(4), 2796–2817 (2024).

[14]S. Ahmadi Seyedkhani, A. Iraji Zad, R. Mohammadpour, M. Taghipoor, and M. Vafaiee, "Novel brain-inspired hierarchical micro-nanostructured poly(3,4-ethylenedioxythiophene)/polydopamine neural interface on titanium nitride electrodes for electrophysiological signal recording," ACS Appl. Bio Mater. **8**, 9332 (2025).

[15]M. Yu, X. Tang, S. Yang, Z. Li, C. Chen, and S. Xie, "Surface functionalized titanium nitride electrode for CMOS compatible bioelectronic devices," ChemMedChem **19**(14), e202400189 (2024).

[16]S. F. Cogan, "Neural stimulation and recording electrodes," Annu. Rev. Biomed. Eng. **10**(1), 275–309 (2008).

[17]M. J. Ebert, S.-P. Lyu, M. T. Rise, and M. F. Wolf, "Biomaterials for pacemakers, defibrillators and neurostimulators," in *Biomaterials for Artificial Organs* (Elsevier, 2011), pp. 81–112.

[18]L. S. Robblee, J. McHardy, W. F. Agnew, and L. A. Bullara, "Electrical stimulation with Pt electrodes. VII. Dissolution of Pt electrodes during electrical stimulation of the cat cerebral cortex," J. Neurosci. Methods **9**(4), 301–308 (1983).

[19]W. F. Agnew, T. G. H. Yuen, D. B. McCreery, and L. A. Bullara, "Histopathologic evaluation of prolonged intracortical electrical stimulation," Exp. Neurol. **92**(1), 162–185 (1986).

[20]S. F. Cogan, A. A. Guzelian, W. F. Agnew, T. G. H. Yuen, and D. B. McCreery, "Over-pulsing degrades activated iridium oxide films used for intracortical neural stimulation," J. Neurosci. Methods **137**(2), 141–150 (2004).

[21]M. Kim, H. Jee, and J. Lee, "Photo-sintered silver thin films by a high-power UV-LED module for flexible electronic applications," Nanomaterials **11**(11), 2840 (2021).

[22]H. Shao, T. Zhang, Y. Gong, and Y. He, "Silver-containing biomaterials for biomedical hard tissue implants," Adv. Healthcare Mater. **12**(26), 2300932 (2023).

[23]K. Stokes, K. Clark, D. Odetade, M. Hardy, and P. Goldberg Oppenheimer, "Advances in lithographic techniques for precision nanostructure fabrication in biomedical applications," Discover Nano **18**(1), 153 (2023).

[24]A. Ramos, V. G. Angel, M. Siqueiros, T. Sahagun, L. Gonzalez, and R. Ballesteros, "Reviewing additive manufacturing techniques: Material trends and weight optimization possibilities through innovative printing patterns," Materials **18**(6), 1377 (2025).

[25]A. F. B. A. Fadzil, A. Pramanik, A. K. Basak, C. Prakash, and S. Shankar, "Role of surface quality on biocompatibility of implants - A review," Ann. 3D Print. Med. **8**, 100082 (2022).

[26]S. Franz, S. Rammelt, D. Scharnweber, and J. C. Simon, "Immune responses to implants – A review of the implications for the design of immunomodulatory biomaterials," Biomaterials **32**(28), 6692–6709 (2011).

[27]W. Yang, Y. Gong, and W. Li, "A review: Electrode and packaging materials for neurophysiology recording implants," Front. Bioeng. Biotechnol. **8**, 622923 (2021).

[28]N. X. Williams, N. Watson, D. Y. Joh, A. Chilkoti, and A. D. Franklin, "Aerosol jet printing of biological inks by ultrasonic delivery," Biofabrication **12**(2), 025004 (2020).

[29]L. De Waele, M. Di Pietro, S. Perilli, E. Mantini, G. Trevisan, M. Simoncini, M. Panella, V. Betti, M. Laffranchi, and D. Mantini, "Aerosol jet printing for neuroprosthetic device development," Bioengineering **12**(7), 707 (2025).

[30]A. J. Capel, M. A. A. Smith, S. Taccola, M. Pardo-Figuerez, R. P. Rimington, M. P. Lewis, S. D. R. Christie, R. W. Kay, and R. A. Harris, "Digitally driven aerosol jet printing to enable customisable neuronal guidance," Front. Cell Dev. Biol. **9**, 722294 (2021).

[31]R. Elsersawy, A. Rahman, C. Sakib-Uz-Zaman, and M. A. H. Khondoker, "Multifunctional inks in aerosol jet printing: Performance, challenges, and applications," Front. Manuf. Technol. **5**, 1558209 (2025).

[32]O. Degryse, V. Bloemen, and E. Ferraris, "Collagen composite inks for aerosol jet® printing in bone tissue engineering applications," Procedia CIRP **110**, 180–185 (2022).

[33]R. Gibney and E. Ferraris, "Bioprinting of collagen type I and II via aerosol jet printing for the replication of dense collagenous tissues," Front. Bioeng. Biotechnol. **9**, 786945 (2021).

[34]M. Nair, E. Inwald, L. Ives, K. R. M. See, and S. Kar-Narayan, "Optimising aerosol jet printing of collagen inks for enhanced piezoelectricity and controlled surface potential," J. Phys. Mater. **6**(3), 034001 (2023).

[35]S. E. Arevalo, D. M. Ebenstein, and L. A. Pruitt, "A methodological framework for nanomechanical characterization of soft biomaterials and polymers," J. Mech. Behav. Biomed. Mater. **134**, 105384 (2022).
[36]L. Mo, Z. Guo, Z. Wang, L. Yang, Y. Fang, Z. Xin, X. Li, Y. Chen, M. Cao, Q. Zhang, and L. Li, "Nano-silver ink of high conductivity and low sintering temperature for paper electronics," Nanoscale Res. Lett. **14**(1), 197 (2019).
[37]H. Ning, Y. Zhou, Z. Fang, R. Yao, R. Tao, J. Chen, W. Cai, Z. Zhu, C. Yang, J. Wei, L. Wang, and J. Peng, "UV-cured inkjet-printed silver gate electrode with low electrical resistivity," Nanoscale Res. Lett. **12**(1), 546 (2017).
[38]A. Efimov, P. Arsenov, D. Kornyushin, A. Lizunova, I. Volkov, and V. Ivanov, "Aerosol jet printing of silver lines with A high aspect ratio on A heated silicon substrate," Materials **13**(3), 730 (2020).
[39]N. Ibrahim, J. O. Akindoyo, and M. Mariatti, "Recent development in silver-based ink for flexible electronics," J. Sci.: Adv. Mater. Devices **7**(1), 100395 (2022).
[40]G. Singh and A. Chanda, "Mechanical properties of whole-body soft human tissues: A review," Biomed. Mater. **16**(6), 062004 (2021).
[41]Y. Shi, R. Liu, L. He, H. Feng, Y. Li, and Z. Li, "Recent development of implantable and flexible nerve electrodes," Smart Mater. Med. **1**, 131–147 (2020).
[42]N. W. Kim, D.-G. Lee, K.-S. Kim, and S. Hur, "Effects of curing temperature on bending durability of inkjet-printed flexible silver electrode," Nanomaterials **10**(12), 2463 (2020).
[43]S. B. Aziz, O. G. Abdullah, D. R. Saber, M. A. Rasheed, and H. M. Ahmed, "Investigation of metallic silver nanoparticles through UV-vis and optical micrograph techniques," Int. J. Electrochem. Sci. **12**(1), 363–373 (2017).
[44]K. C. Song, S. M. Lee, T. S. Park, and B. S. Lee, "Preparation of colloidal silver nanoparticles by chemical reduction method," Korean J. Chem. Eng. **26**(1), 153–155 (2009).
[45]N. Bogdanchikova, "On the nature of the silver phases of Ag/Al_2O_3 catalysts for reactions involving nitric oxide," Appl. Catal., B **36**(4), 287–297 (2002).
[46]D. Chen, Z. Qu, S. Shen, X. Li, Y. Shi, Y. Wang, Q. Fu, and J. Wu, "Comparative studies of silver based catalysts supported on different supports for the oxidation of formaldehyde," Catal. Today **175**(1), 338–345 (2011).
[47]Z.-m. Xiu, Q.-b. Zhang, H. L. Puppala, V. L. Colvin, and P. J. J. Alvarez, "Negligible particle-specific antibacterial activity of silver nanoparticles," Nano Lett. **12**(8), 4271–4275 (2012).
[48]M. Nair (2026). "Research data supporting 'Aerosol jet co-printing for flexible and conductive protein-metal electrodes'," University of Oxford, Dataset. https://doi.org/10.5287/ora-14x9dqqzp